

# PCCP

Accepted Manuscript

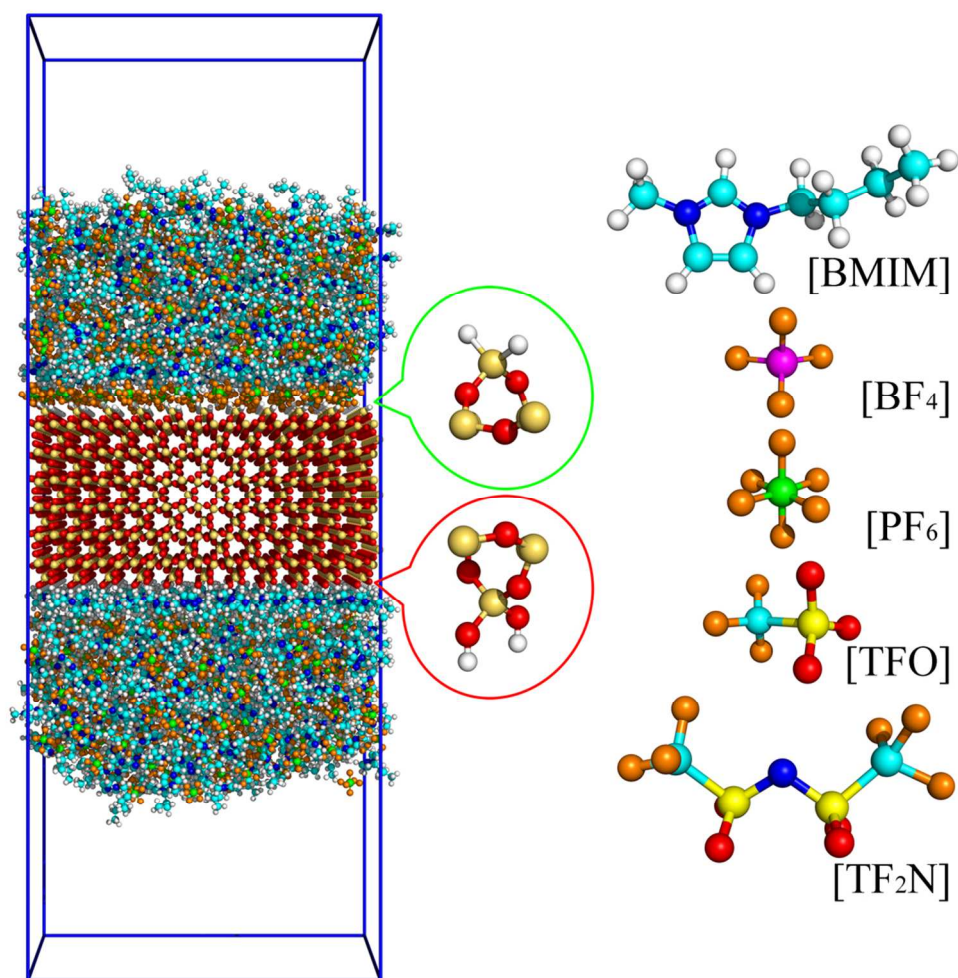


This is an *Accepted Manuscript*, which has been through the Royal Society of Chemistry peer review process and has been accepted for publication.

*Accepted Manuscripts* are published online shortly after acceptance, before technical editing, formatting and proof reading. Using this free service, authors can make their results available to the community, in citable form, before we publish the edited article. We will replace this *Accepted Manuscript* with the edited and formatted *Advance Article* as soon as it is available.

You can find more information about *Accepted Manuscripts* in the [Information for Authors](#).

Please note that technical editing may introduce minor changes to the text and/or graphics, which may alter content. The journal's standard [Terms & Conditions](#) and the [Ethical guidelines](#) still apply. In no event shall the Royal Society of Chemistry be held responsible for any errors or omissions in this *Accepted Manuscript* or any consequences arising from the use of any information it contains.



Interfacial Structure and Orientation of Confined Ionic Liquids on Charged Quartz Surfaces

# Interfacial structure and orientation of confined ionic liquids on charged quartz surfaces

Yong-Lei Wang<sup>\*a</sup> and Aatto Laaksonen<sup>\*a,b</sup>

Received Xth XXXXXXXXXXXX 20XX, Accepted Xth XXXXXXXXXXXX 20XX

First published on the web Xth XXXXXXXXXXXX 200X

DOI: 10.1039/b000000x

Atomistic molecular dynamics simulations have been performed to study microscopic ionic structures and orientational preferences of absorbed [BMIM] cations and four paired anions ([BF<sub>4</sub>], [PF<sub>6</sub>], [TFO] and [TF<sub>2</sub>N]) on quartz surfaces. Two chemically different quartz surface models were adopted: one is saturated with silanol Si(OH)<sub>2</sub> groups, and the other one is covered by silane SiH<sub>2</sub> groups, respectively. Simulation results reveal that dense ionic layers, characterized by distinct mass, number, charge and electron densities, are formed in quartz interfacial region. The orientational preferences of confined ionic groups are characterized with different features depending on the size and shape of anionic groups, and the quartz surface charge. The [BMIM] cations attach exclusively onto the negatively charged Si(OH)<sub>2</sub> surface. The imidazolium rings lie preferentially perpendicular to Si(OH)<sub>2</sub> surface, to which the directly connected methyl and butyl chains are oriented and elongated along Si(OH)<sub>2</sub> surface, respectively. The anions are mainly absorbed on positively charged SiH<sub>2</sub> surface. The main axes of asymmetric [TFO] and [TF<sub>2</sub>N] anions are perpendicular and parallel to SiH<sub>2</sub> surface, respectively. Such distinct structural and orientational preferences of confined ionic groups attribute to the strong electrostatic interactions and the formation of hydrogen bonds between confined ionic species and quartz interfacial groups.

## 1 Introduction

Investigations of structural and dynamical properties of room temperature ionic liquids (ILs) under confinement are of key interest in many potentially promising applications, such as catalysis<sup>1–3</sup>, electrochemistry<sup>4,5</sup>, microlubrication and nanotribology<sup>6–12</sup>, and multiphase separation<sup>13–15</sup>, where ILs are recognized to be fascinating alternatives to traditional molecular solvents. The physicochemical properties of ILs confined within a solid matrix are quite different from those in the corresponding bulk systems. Many striking phenomena have been reported concerning the effect of nanoconfinement on the change in melting points<sup>16–23</sup>, crystal structures<sup>16,18,24</sup>, and chemical reactivities<sup>25</sup> of confined ionic species.

Most of the current understanding on interfacial microscopic ionic structures of confined ILs is obtained experimentally from atomic force microscopy (AFM)<sup>10,11,24,26,27</sup>, direct recoil spectroscopy<sup>28,29</sup>, X-ray and neutron reflectivity<sup>30–33</sup>, sum frequency generation (SFG) vibrational spec-

troscopy<sup>32,34–42</sup>, and computationally by atomistic<sup>43–45</sup> and coarse-grained simulations<sup>46–49</sup>. For ionic groups confined inside neutral multiwalled carbon nanotubes<sup>16,18,50</sup> or on multilayered graphene surfaces<sup>23,45,51</sup>, a distinct structural transition from liquid to solid or crystal may take place, owing to the particular molecular orientation of confined ILs triggered by strong and complex interactions between ILs and solid surfaces. The distribution and orientation of absorbed ILs on charged solid surfaces<sup>10,17,52–57</sup> are distinct compared to those absorbed on neutral solid surfaces. Experimental evidence has already demonstrated the coexistence of liquid and crystalline phases of confined [BMIM][PF<sub>6</sub>] IL on atomically flat mica surface at room temperature using AFM technique<sup>52</sup>. The crystalline structure of [BMIM][PF<sub>6</sub>] is stable and undisturbed by the force applied in AFM measurement. Subsequent experiments revealed that a variety of protic and aprotic ILs exhibit strong interfacial stacking phenomena described by interdigitated cationic and anionic layers in the vicinity of charged solid surfaces<sup>17,53,54,56,57</sup>. These interdigitated ionic layers decay exponentially into bulk liquid phase. The observed decay length and layering period point to an interfacial ordering mechanism, akin to the charge inversion effect, which is rationalized by the strong correlations between absorbed ionic species and charged solid surfaces<sup>17</sup>. Such observed layering phenomena, verified both in AFM experiments<sup>17,52,53,56</sup> and molecular simulations<sup>46–48,57</sup>, are expected to be a generic feature of confined ILs on charged solid surfaces.

<sup>a</sup> Department of Materials and Environmental Chemistry, Arrhenius Laboratory, Stockholm University, Stockholm S-106 91, Sweden. E-mail: yonglei.wang@mmk.su.se; aatto.laaksonen@mmk.su.se.

<sup>b</sup> Stellenbosch Institute of Advanced Studies (STIAS), Wallenberg Research Center, Stellenbosch University, Stellenbosch 7600, South Africa.

† Electronic Supplementary Information (ESI) available: Force field parameters of [BMIM] cation, [BF<sub>4</sub>], [PF<sub>6</sub>], [TFO] and [TF<sub>2</sub>N] anions; Force field parameters of atomistic quartz Si(OH)<sub>2</sub> and SiH<sub>2</sub> surface models; Functional form of potential energy; See DOI: 10.1039/b000000x/

Besides the formation of interfacial layering ionic structures, the microscopic distribution and orientation of confined ILs are of paramount importance for energy storage devices<sup>13,58–60</sup>, particularly for those taking advantage of IL electrolytes to store energy. Numerous experiments have suggested that the distribution and orientation of imidazolium-based ILs on charged quartz surfaces intrinsically depend on ionic size and molecular geometry of anionic groups, the alkyl chain length of cations, as well as the water content in IL samples and gas phase<sup>21,22,26,35,38,39,40,43,61–67</sup>. The AFM measurements have revealed that the formation of solvation IL layers on quartz surfaces is strongly related to quartz surface charge and roughness<sup>24,26,27,39,40</sup>. The SFG vibrational spectroscopic signature indicated that imidazolium rings prefer to lie on quartz surfaces with the attached alkyl chains taking on tilted orientation<sup>35,38–40</sup>. However, this qualitative conclusion was drawn based on the simple assumption that each confined cation behaves more or less as a rigid entity, and the limited molecular-level information on the average orientation of “reporter” groups, such as the vibration frequency of aromatic C–H bonds on imidazolium rings<sup>21,35,38,39,42,67</sup>. Due to the lack of spectroscopic signature, the distribution and orientation of anionic groups were not directly investigated. The intrinsic relationship between the specific orientation of confined ILs in interfacial region and the precise nature of quartz surfaces was not clearly identified either. Computer simulations on IL systems represented at the atomic level, on the other hand, can provide valuable microscopic insight of detailed ionic structures and orientational preferences of confined ILs in quartz interfacial region at well-defined conditions.

In present work, atomistic molecular dynamics simulations are performed to investigate the interfacial ionic structures of confined ILs on charged quartz surfaces. Four simulation systems consisting of [BMIM] cations paired with [BF<sub>4</sub>], [PF<sub>6</sub>], [TFO] and [TF<sub>2</sub>N] anions are considered in present simulations due to their popularization in fundamental and industrial applications. The intrinsic distribution and orientation of confined ILs in quartz interfacial region, as well as the formation of particular solvation pattern as a function of relative distance from quartz surfaces, are analyzed in detail.

## 2 Quartz models and simulation methodology

In present atomistic simulations, a silica hexagonal unit cell with dimensions of  $0.4913 \times 0.5405 \text{ nm}^2$  is adopted from structural database of Accelrys Materials Studio software. The quartz periodic structure is built by stacking this unit cell 7 times along the Z axis to obtain a representative configuration with approximately 2.9 nm in thickness, and then repeating such representative structure  $11 \times 10$  times along the XY plane, leading to two quartz surfaces characterized with  $5.4043 \times 5.4052 \text{ nm}^2$ . Two different surface saturation

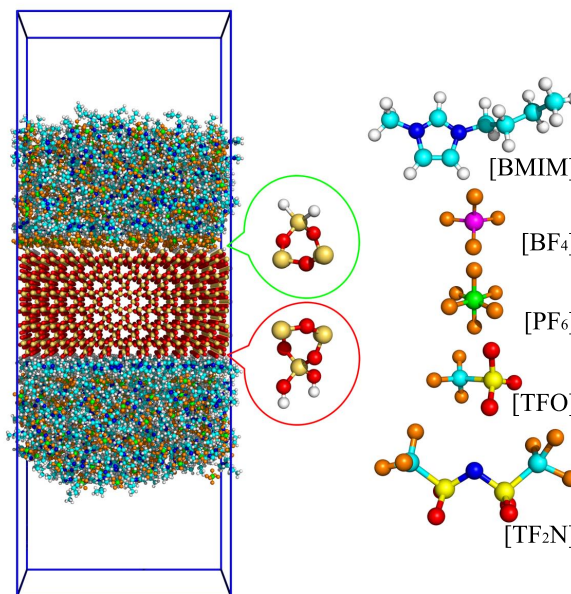


**Fig. 1** Right: Molecular structures of [BMIM] cation, [BF<sub>4</sub>], [PF<sub>6</sub>], [TFO], and [TF<sub>2</sub>N] anions. Left: Representative configuration of absorbed [BMIM][PF<sub>6</sub>] ion pairs on Si(OH)<sub>2</sub> (bottom) and SiH<sub>2</sub> (top) surfaces.

schemes are considered to mimic synthesized and catalytic quartz surface models<sup>21,22,38,68–71</sup>. In one exposed quartz surface, the dangling silicon atoms are saturated with silanol hydroxyl groups, resulting this surface in full coverage of 110 Si(OH)<sub>2</sub> groups, whereas the other one is fully hydrogenated and covered by 110 silane SiH<sub>2</sub> groups, respectively. The so-constructed quartz structure is parallel to the XY plane and kept frozen in all simulation systems. The procedure of building the initial configuration of confined ILs on Si(OH)<sub>2</sub> and SiH<sub>2</sub> surfaces is similar to that adopted in previous work<sup>45</sup>. Two IL films, each one of which consists of 256 ion pairs, are absorbed on Si(OH)<sub>2</sub> and SiH<sub>2</sub> surfaces in the corresponding simulation systems. The representative configuration of absorbed [BMIM][PF<sub>6</sub>] ion pairs on Si(OH)<sub>2</sub> and SiH<sub>2</sub> surfaces is shown in Fig. 1.

The atomistic force field developed by MacKerell and coworkers with additional parameters specifically tailored for Si(OH)<sub>2</sub> and SiH<sub>2</sub> surfaces<sup>72</sup> is adopted in present work to model bulk quartz and quartz surfaces. The atomic partial charges of quartz atoms are derived from electrostatic potential fitting of the representative configuration described above using Gaussian 09 package<sup>73</sup> at B3LYP/6-31+G(d) level. The derived atomic partial charges are set equal to all same type atoms in quartz structure, and are listed in the ESI. The force field parameters of atomistic [BMIM] cation and paired anions stem from a systematically improved force field, in which

both inter- and intra- molecular interaction parameters were refined to achieve quantitative description of intermolecular ionic structures obtained from quantum chemistry *ab initio* calculations, and tuned to fit vibration frequency data obtained from experiments, respectively<sup>74,75</sup>. Such an improved force field, as shown in previous work<sup>76,77</sup>, could reproduce good thermodynamic, structural and scattering properties of studied ILs. The detailed force field parameters of [BMIM] cation and four paired anions, as well as the corresponding functional form for potential energy, are provided in the ESI.

Atomistic molecular dynamics simulations are performed using M.Dynamix package<sup>78</sup> with standard three-dimensional periodic boundary condition. The periodic distance in the Z axis, which is perpendicular to quartz surfaces, is set to 18.0 nm, which is sufficiently large so that the interactions between absorbed ILs on Si(OH)<sub>2</sub> surface and those confined on SiH<sub>2</sub> surface can be ignored. The equations of motion are integrated using the Tuckerman-Berne double time step algorithm<sup>79</sup> with short and long time steps of 0.2 and 2.0 fs, respectively. The short time step is used for integrating fast intramolecular vibrations and nonbonded interactions within 0.5 nm, while the long time step is used for integrating van der Waals and electrostatic interactions within 1.5 nm, as well as dihedral angle motions. The electrostatic interactions between atom-centered point charges are treated with standard Ewald summation method. All equilibrated systems are simulated in NVT ensemble at 300 K maintained using Nosé-Hoover thermostat. The production phase persists 8 ns, in which trajectories are saved at an interval of 100 fs for further analysis.

### 3 Results and Discussion

The discussion of microscopic ionic structures of confined ILs on solid surfaces usually involves two different but inter-related aspects, namely, the chemical composition and molecular orientation of absorbed ILs in interfacial region. The former one is used to identify and characterize the relative enhancement and depletion of certain physical property of confined ILs in interfacial region with respect to bulk system. In following parts, the interfacial chemical composition, characterized by mass, number, charge and electron density distributions in Si(OH)<sub>2</sub> and SiH<sub>2</sub> interfacial regions, are discussed in detail. Furthermore, the molecular orientations of specific vectors fixed in [BMIM] cation frame, and in asymmetric [TFO] and [TF<sub>2</sub>N] anions in quartz interfacial region, are examined by calculating the corresponding probability distributions.

#### 3.1 Mass and number density distributions

The individual mass density profiles of [BMIM] cations and paired anions, as well as the total mass density distribu-

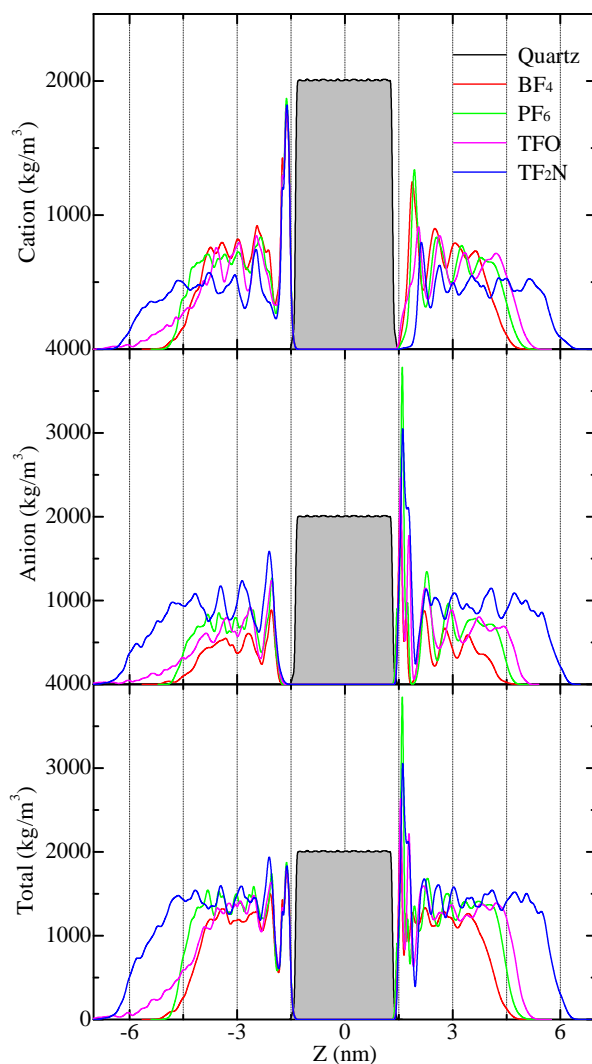


**Fig. 2** The individual and total mass density profiles of [BMIM] cations and paired anions normal to Si(OH)<sub>2</sub> and SiH<sub>2</sub> surfaces.

tions normal to Si(OH)<sub>2</sub> and SiH<sub>2</sub> surfaces, are presented in Fig. 2. The grey area represents the bulk quartz, in which the left and right surfaces are saturated with Si(OH)<sub>2</sub> and SiH<sub>2</sub> groups and are characterized by negative and positive charges, respectively, leading to the distinct stacking behavior of confined ILs on these two quartz surfaces. The remarkably pronounced mass density distributions in quartz interfacial region indicate the formation of dense ionic layers. The formation of interfacial high-density domain is, not only triggered by quartz surfaces<sup>24,27,43,63,64,67,80</sup>, but also induced by other charged<sup>26,46,56</sup> or neutral<sup>23,44,45,56,81,82</sup> solid surfaces.

In Si(OH)<sub>2</sub> interfacial region, the total mass density profiles are characterized with double intermediate peaks, indicating the formation of double ionic layers. On further inspection,

it is observed that the total mass density distributions of these two layers come from different ionic group contribution. The local maxima of [BMIM] cationic mass density profiles coincide with the local minima of anionic mass density profiles and *vice versa*, implying that the first ionic layer adsorbed on  $\text{Si}(\text{OH})_2$  surface is exclusively consisting of [BMIM] cations, and the subsequent layer is mainly consisting of paired anions, respectively. Each layer is approximately 0.45 nm in thickness, as illustrated from the pronounced out-of-phase oscillations in the corresponding mass density profiles. Beyond these two layers in  $\text{Si}(\text{OH})_2$  interfacial region, both individual and total mass density profiles exhibit little fluctuation in bulk region of confined films.

The mass density profiles of [BMIM] cations and paired anions show a similar tendency in  $\text{SiH}_2$  interfacial region, but with different characteristics. The first layer on  $\text{SiH}_2$  surface is particularly consisting of anionic groups, and the effective thickness of such layer increases with the increase of anionic size, as verified in AFM experiments<sup>27</sup> and atomistic simulations<sup>27,65</sup>. The sharp peaks in anionic mass density profiles attribute to the most probable distribution of adsorbed anions on  $\text{SiH}_2$  surface<sup>45,81,83</sup>. The subsequent layer in  $\text{SiH}_2$  interfacial region mainly consists of [BMIM] cations, of which the mass density profiles are characterized by broad and less intensive peaks compared to the sharp mass density distributions in  $\text{Si}(\text{OH})_2$  interfacial region. The most popular distribution position in these mass density profiles gradually shifts to large distance with the increase of anionic size.

Beyond the high-density domain in  $\text{SiH}_2$  interfacial region, both cationic and anionic mass density profiles exhibit damped oscillations in [BMIM][ $\text{BF}_4$ ], [BMIM][ $\text{PF}_6$ ] and [BMIM][TFO] simulation systems, which extend to more than 1.5 nm with at least three non-negligible ionic layers. The interdigitated mass density profiles of [BMIM] cations and paired anions suggest the formation of alternating local ionic structures. In contrast, both [BMIM] cations and [ $\text{TF}_2\text{N}$ ] anions exhibit smooth mass density distributions with a weak fluctuation beyond interfacial high-density domain, as well as the total mass density distribution even minor oscillation is observed in bulk region of confined films. Such striking phenomena attribute to the relatively large ionic size and flexible molecular conformation of [ $\text{TF}_2\text{N}$ ] anions, which contribute to the distinct distribution and orientation of [ $\text{TF}_2\text{N}$ ] anions on  $\text{SiH}_2$  surface.

To understand more detailed microscopic ionic structures in quartz interfacial region, the number density distributions of confined ILs are calculated and shown in Fig. 3. Panels (a) and (b) show the number densities of the geometrical centers of imidazolium rings, and the terminal carbon atoms in methyl (Cm) and butyl chains (Cb) of [BMIM] cations, respectively. Panel (c) presents number densities of boron (B) and phosphorus (P) atoms in symmetric [ $\text{BF}_4$ ] and [ $\text{PF}_6$ ] anions. The

number densities of specific atoms in asymmetric [TFO] and [ $\text{TF}_2\text{N}$ ] anions are shown in panel (d).

As expected from the mass density distributions, the number densities of confined ILs exhibit similar pronounced oscillations. Both imidazolium rings and Cm atoms display single and sharply pronounced distributions in  $\text{Si}(\text{OH})_2$  interfacial region. The main distribution of Cm atoms locates between that of imidazolium rings and  $\text{Si}(\text{OH})_2$  surface, signifying a depletion of methyl groups in  $\text{Si}(\text{OH})_2$  interfacial region. The number densities of Cb atoms are characterized by multiple peaks, attributing to the flexible conformation of butyl chains, in contrast to the exclusive parallel orientation of butyl chains along flat graphene surface<sup>45,84,85</sup>. A subtle character presented in the number density profiles of Cb atoms is that the most probable distribution locates between the main and secondary distributions of imidazolium rings, as shown in panel (a), and consistent with that of anionic groups shown in panels (c) and (d) of Fig. 3. Such distribution pattern corresponds to the formation of winding sheet structures of imidazolium rings between which the interdigitated butyl chains and anionic groups are sandwiched.

For the number densities of B and P atoms of adsorbed [ $\text{BF}_4$ ] and [ $\text{PF}_6$ ] anions shown in panel (c), and that of sulphur (S) and carbon (C) atoms of [TFO] anions presented in panel (d) of Fig. 3, single pronounced peak and subsequent damped multiple peaks are observed in  $\text{Si}(\text{OH})_2$  interfacial region. While in [BMIM][ $\text{TF}_2\text{N}$ ] simulation system, the multiple peaks with intermediate intensity in number density profiles of nitrogen (N), S and C atoms of [ $\text{TF}_2\text{N}$ ] anions indicate the alternating distribution of [ $\text{TF}_2\text{N}$ ] anions on  $\text{Si}(\text{OH})_2$  surface, implying a strong ion effect in  $\text{Si}(\text{OH})_2$  interfacial region.

In contrast, the exclusive stacking of anionic groups on  $\text{SiH}_2$  surface contributes to the sharp pronounced number density distributions, as shown in panels (c) and (d) of Fig. 3. The damped number densities of symmetric [ $\text{BF}_4$ ] and [ $\text{PF}_6$ ] anions indicate the formation of staged ionic structures in  $\text{SiH}_2$  interfacial region. For asymmetric [TFO] and [ $\text{TF}_2\text{N}$ ] anions, the distribution of S atoms is much closer to  $\text{SiH}_2$  surface than that of C atoms, indicating the perpendicular or tilted orientation of S-C covalent bonds with respect to  $\text{SiH}_2$  surface. The most probable distribution of N atoms in [ $\text{TF}_2\text{N}$ ] anions is found between that of S and C atoms, implying that  $\text{SO}_2$  groups locate close to and  $\text{CF}_3$  groups away from  $\text{SiH}_2$  surface, respectively, which is similar to the distribution of [ $\text{TF}_2\text{N}$ ] anions on charged alumina<sup>17,86</sup> and neutral graphene surfaces<sup>81</sup>.

For [BMIM] cations on  $\text{SiH}_2$  surface, imidazolium rings and terminal carbon atoms in methyl and butyl chains exhibit different number densities compared to those in  $\text{Si}(\text{OH})_2$  interfacial region. The imidazolium rings mainly contribute to the cationic layer, and their main distribution in such layer

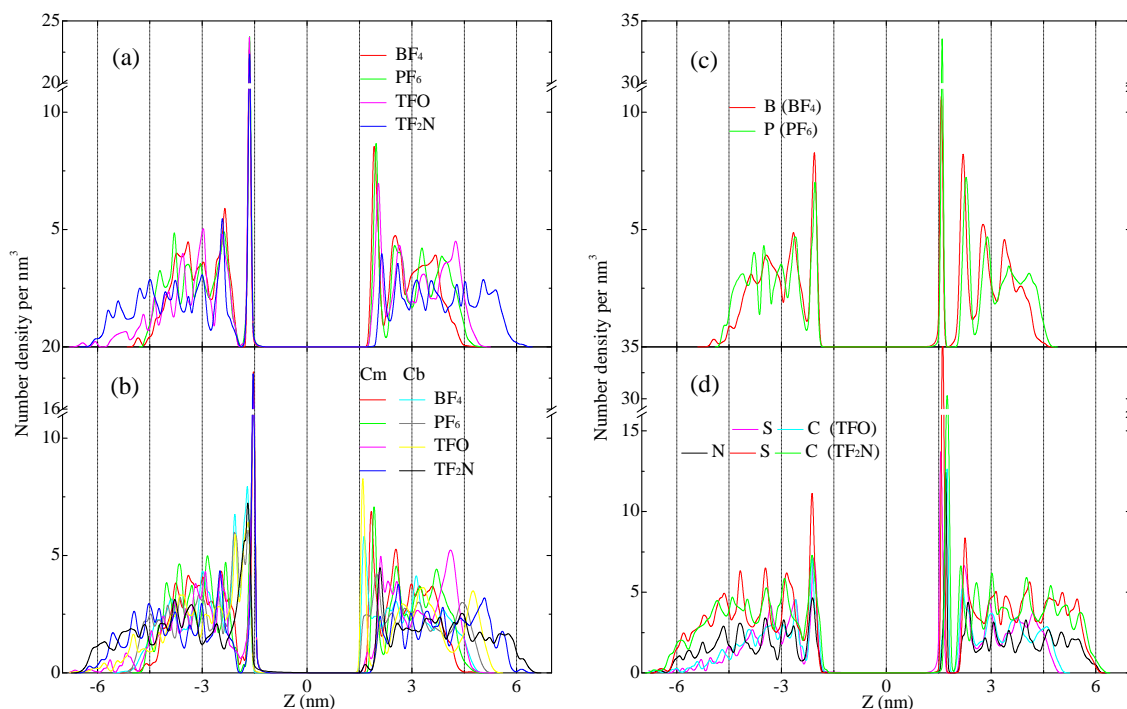


**Fig. 3** Number density distributions of [BMIM] cations and paired anions normal to  $\text{Si(OH)}_2$  and  $\text{SiH}_2$  surfaces. (a) Geometrical center of imidazolium ring; (b) Terminal carbon atoms in methyl (Cm) and butyl chains (Cb) of [BMIM] cation; (c) Geometrical central atoms of symmetric  $[\text{BF}_4]$  and  $[\text{PF}_6]$  anions; (d) Representative atoms of asymmetric [TFO] and  $[\text{TF}_2\text{N}]$  anions.

gradually shifts to large distance with the increase of anionic size. In  $[\text{BMIM}][\text{BF}_4]$  and  $[\text{BMIM}][\text{TFO}]$  simulation systems, the main distribution of Cb atoms is adjacent to  $\text{SiH}_2$  surface, and comparable to that of B and S atoms in  $[\text{BF}_4]$  and [TFO] anions, respectively. However in  $[\text{BMIM}][\text{PF}_6]$  and  $[\text{BMIM}][\text{TF}_2\text{N}]$  simulation systems, both Cm and Cb atoms exhibit similar number densities, indicating a parallel orientation of butyl chain along  $\text{SiH}_2$  surface in the cationic layer.

### 3.2 Charge and electron density distributions

The variation of individual and total volume charge densities of confined ILs in quartz interfacial region are presented in Fig. 4. It is clearly shown that the quartz surfaces saturated with  $\text{Si(OH)}_2$  and  $\text{SiH}_2$  groups are characterized by negative and positive charges, respectively. Such intrinsic difference in local chemical composition and surface charge leads to distinct stacking behavior of absorbed ILs on these two quartz surfaces, as addressed in previous subsection. In all volume charge density profiles, the spatial inhomogeneous domain shows similar pronounced pattern in quartz interfacial region, but with less extended oscillations compared to mass and number density profiles. The absorbed ILs on charged quartz surfaces normally can screen a major part of the surface charge, leading to a quick recovery of volume charge density

to bulk value with the increase of their relative distance to quartz surfaces, which is consistent with Baldelli's experimental results<sup>87</sup>.

The pronounced volume charge densities in  $\text{Si(OH)}_2$  interfacial region attribute to the distinct orientation of absorbed [BMIM] cations. In  $\text{SiH}_2$  interfacial region, the double valleys in total volume charge densities of  $[\text{BMIM}][\text{BF}_4]$  and  $[\text{BMIM}][\text{PF}_6]$  simulation systems imply the strongly coupled ionic structures between [BMIM] cations and paired symmetric anions through electrostatic interactions, as indicated in damped number density profiles in panel (c) of Fig. 3. For asymmetric [TFO] and  $[\text{TF}_2\text{N}]$  anions, the distinct total volume charge densities are only embodied in high-density domain in  $\text{SiH}_2$  interfacial region. Such volume charge density arrangement is rationalized by complex microscopic ionic structures, which arise from the most probable orientation of absorbed ILs in  $\text{SiH}_2$  interfacial region. The damped charge density profiles and associated ionic structures demonstrate the pronounced charge overscreening phenomena, *i.e.*, excess charges in the first ionic layer with respect to adjacent surface charges, which highlight the critical role of charge-induced nanoscale correlations in confined IL films. The present simulation results, together with previous X-ray scattering experimental data<sup>56</sup>, verify the key aspect of a predicted electric

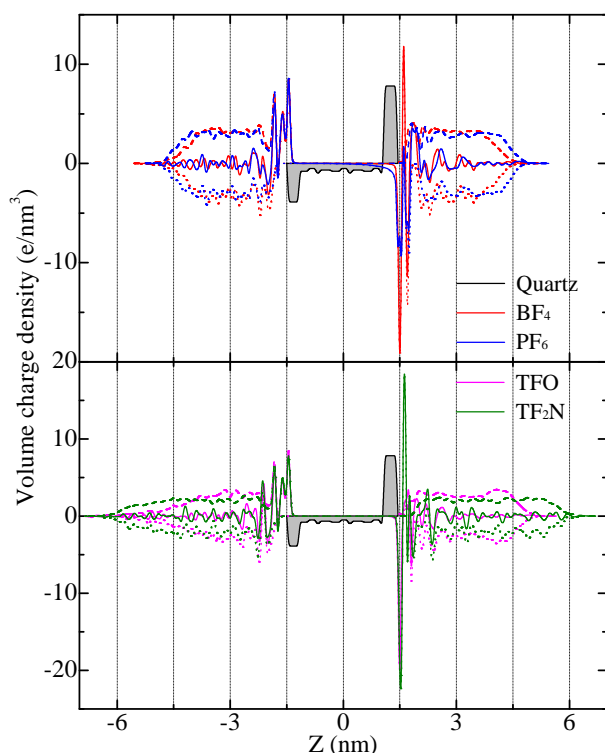


**Fig. 4** The variation of individual volume charge densities of [BMIM] cations (dashed lines) and paired anions (dotted lines), as well as the total volume charge densities (solid lines) normal to  $\text{Si}(\text{OH})_2$  and  $\text{SiH}_2$  surfaces. The grey area represents the volume charge densities of quartz, in which the left and right surfaces are covered by  $\text{Si}(\text{OH})_2$  and  $\text{SiH}_2$  groups and are characterized by negative and positive charges, respectively.

double-layer structure from an analytical Landau-Ginzburg-type continuum theory incorporating ion correlation effect<sup>88</sup>.

Besides the mass, number and charge densities, another valuable characterization of confined ILs is the volume electron density, which can be directly measured from X-ray reflectivity experiments<sup>31,62,89</sup>. In present simulations, the variation of individual and total volume electron densities of [BMIM] cations and paired anions in quartz interfacial region are calculated and shown in Fig. 5.

Similar interdigitated and damped total volume electron density distributions are observed in quartz interfacial region, which mirror the observed number density distributions in the corresponding simulation systems. But the individual volume electron densities of [BMIM] cations and paired anions exhibit distinct features in bulk region of confined films. The individual contribution of [BMIM] cations, either in  $\text{Si}(\text{OH})_2$  or in  $\text{SiH}_2$  interfacial regions, is much larger than that of  $[\text{BF}_4]$  anions, but comparable to that of  $[\text{PF}_6]$  anions in the corresponding simulation systems. Such different individual contri-

butions in bulk region of confined films, which have the same [BMIM] cations, stem from the ionic size and number of electrons of respective anions. The ionic radii of  $[\text{BF}_4]$  and  $[\text{PF}_6]$  anions are approximately 0.220 nm and 0.276 nm, resulting in the corresponding electron densities around  $0.92 \times 10^3 \text{ e/nm}^3$  and  $0.78 \times 10^3 \text{ e/nm}^3$ , respectively<sup>31</sup>. As the number fraction of [BMIM] cations in bulk region is 0.5 because of the charge neutrality, the bulk volume fractions are estimated to be 0.14 and 0.25 for  $[\text{BF}_4]$  and  $[\text{PF}_6]$  anions, respectively<sup>31</sup>, leading to the smaller contribution of  $[\text{BF}_4]$  anions than  $[\text{PF}_6]$  anions to total electron densities in bulk region of confined films. The total electron densities of [BMIM] $[\text{BF}_4]$  and [BMIM] $[\text{PF}_6]$  ILs, estimated from bulk region of confined films, are approximately  $0.385 \times 10^3 \text{ e/nm}^3$  and  $0.427 \times 10^3 \text{ e/nm}^3$ , respectively. Both of them are quite close to the X-ray reflectivity experimental data of  $0.38 \times 10^3 \text{ e/nm}^3$  and  $0.42 \times 10^3 \text{ e/nm}^3$ , respectively, of the corresponding simulation systems<sup>31</sup>.

In panels (c) and (d) of Fig. 5, the individual contributions of asymmetric [TFO] and  $[\text{TF}_2\text{N}]$  anions are approximately  $0.198 \times 10^3 \text{ e/nm}^3$  and  $0.242 \times 10^3 \text{ e/nm}^3$ , respectively. These values are consistent with those estimated from bulk volume fractions and ionic radii of [TFO] and  $[\text{TF}_2\text{N}]$  anions deduced from quantum chemistry calculations<sup>90</sup>. Such different contributions of anions, in turn, affect the individual contribution of [BMIM] cations to total electron densities in bulk region of confined films.

### 3.3 Orientational preferences

Having specified the distinct density distributions on  $\text{Si}(\text{OH})_2$  and  $\text{SiH}_2$  surfaces, we proceed to examine the detailed molecular orientational characteristics of absorbed ILs in quartz interfacial region. The probability distribution is described by the first Legendre polynomial as  $P_1(\cos\theta) = \langle \cos\theta \rangle$ , where  $\theta$  is the angle between a specific vector and positive Z-axis. The probability distributions of specific vectors fixed in [BMIM] cation frame, such as imidazolium ring normal, CR-H5 and Nm-Nb vectors, are presented in Fig. 6. The joint probability distribution of these three vectors can accurately characterize the intrinsic orientation of imidazolium ring in quartz interfacial region.

The experimental SFG spectra revealed that in confined [BMIM] $[\text{BF}_4]$  and [BMIM] $[\text{PF}_6]$  films on  $\text{Si}(\text{OH})_2$  surface, the tilt angle of imidazolium ring is  $45^\circ - 90^\circ$ , with possible twist angle of  $0^\circ - 30^\circ$ <sup>38</sup>. Coasne and coworkers found that both imidazolium rings and alkyl chains of absorbed [BMIM] $[\text{TF}_2\text{N}]$  ion pairs inside a hydroxylated amorphous silica nanopore prefer perpendicular orientations to silica surface through computer simulations<sup>67</sup>. In present atomistic simulations, the orientation of imidazolium ring normal, either on negatively charged  $\text{Si}(\text{OH})_2$  surface or on positively charged  $\text{SiH}_2$  surface, indicates that the imidazolium ring ex-

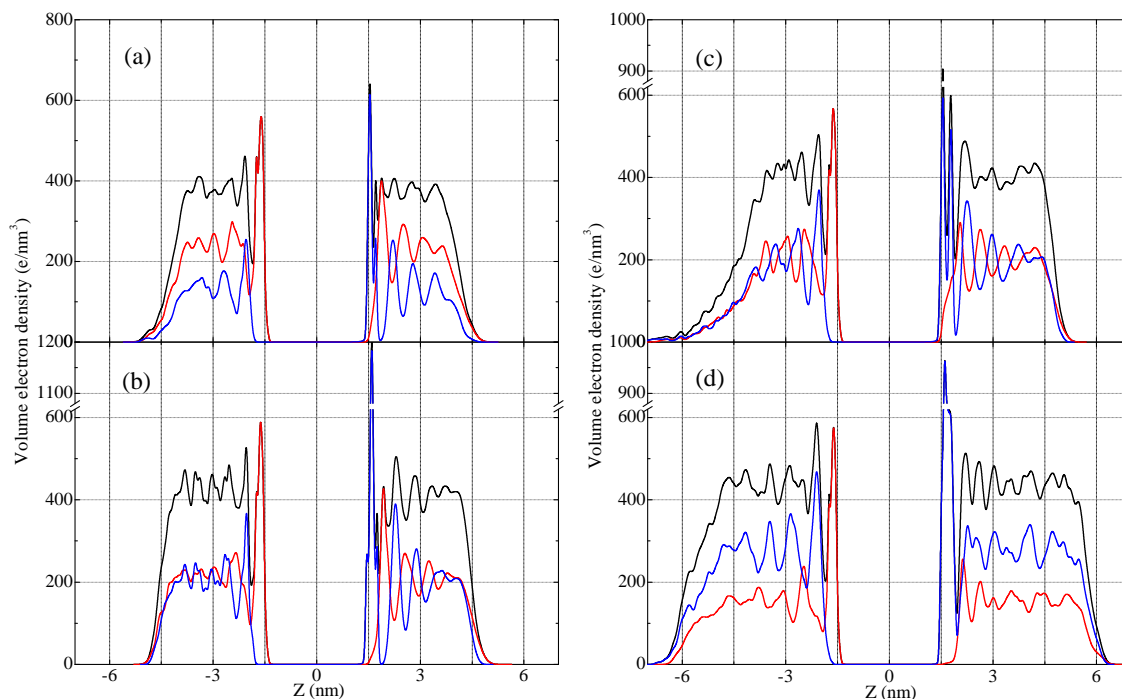


**Fig. 5** The variation of individual volume electron densities of [BMIM] cations (red) and paired anions (blue), as well as the total volume electron density distributions (black) normal to  $\text{Si}(\text{OH})_2$  and  $\text{SiH}_2$  surfaces. (a) [BMIM][ $\text{BF}_4$ ]; (b) [BMIM][ $\text{PF}_6$ ]; (c) [BMIM][TFO]; (d) [BMIM][ $\text{TF}_2\text{N}$ ].

hibits exclusive perpendicular orientation in quartz interfacial region. But the varied probability distributions of CR-H5 and Nm-Nb vectors imply that the orientational preferences of imidazolium rings on  $\text{Si}(\text{OH})_2$  and  $\text{SiH}_2$  surfaces are distinct with different atoms close to quartz surfaces.

On  $\text{Si}(\text{OH})_2$  surface, the angle between CR-H5 vector and positive Z-axis is approximately  $10^\circ$ , indicating that all CR-H5 vectors (as well as imidazolium rings) are essentially perpendicular to  $\text{Si}(\text{OH})_2$  surface with H5 atoms close to  $\text{Si}(\text{OH})_2$  groups, leading to the parallel orientation of Nm-Nb vector along  $\text{Si}(\text{OH})_2$  surface. The secondary peaks in CR-H5 probability distribution profiles indicate that few vectors take on tilted orientation with approximately  $50^\circ$  from  $\text{Si}(\text{OH})_2$  surface, consistent with similar secondary peaks in Nm-Nb probability distribution profiles and related experimental SFG spectra of confined [BMIM][ $\text{BF}_4$ ] and [BMIM][ $\text{PF}_6$ ] ILs<sup>38</sup>.

The anionic groups are particularly absorbed in  $\text{SiH}_2$  interfacial region due to strong electrostatic interactions, which prevent imidazolium rings from approaching  $\text{SiH}_2$  surface, leading to their aggregations beyond interfacial region. Even the sharp distribution of imidazolium ring normal is similar to that in  $\text{Si}(\text{OH})_2$  interfacial region, the varied probability distributions of CR-H5 and Nm-Nb vectors imply that the most probable orientation of imidazolium ring is affected by ionic size and molecular geometry of anionic groups.

In [BMIM][ $\text{BF}_4$ ] and [BMIM][ $\text{PF}_6$ ] simulation systems, imidazolium rings in  $\text{SiH}_2$  interfacial region take on similar orientation as those in  $\text{Si}(\text{OH})_2$  interfacial region, as validated by the joint probability distribution of imidazolium ring normal, CR-H5 and Nm-Nb vectors. For imidazolium rings in [BMIM][TFO] simulation system, a majority of Nm-Nb vectors are generally perpendicular to  $\text{SiH}_2$  surface and some of them are approximately  $25^\circ$  away from  $\text{SiH}_2$  surface, with the corresponding CR-H5 vectors taking on random distributions in  $\text{SiH}_2$  interfacial region. While in [BMIM][ $\text{TF}_2\text{N}$ ] simulation system, CR-H5 vector is approximately  $17^\circ$  away from  $\text{SiH}_2$  surface with H5 atoms pointing into neighboring anionic layer, which lies between the subsequent cationic layer and  $\text{SiH}_2$  surface. Typical configuration of imidazolium rings in  $\text{Si}(\text{OH})_2$  and  $\text{SiH}_2$  interfacial regions is shown in Fig. 7.

One important reason for the distinct orientation of CR-H5 vector in quartz interfacial region attributes to the formation of hydrogen bonds between H5 and polar atoms in anionic groups, as well as interfacial oxygen (O) atoms on  $\text{Si}(\text{OH})_2$  surface<sup>21</sup>. The exclusive stacking of [BMIM] cations on  $\text{Si}(\text{OH})_2$  surface and the sharp perpendicular orientation of CR-H5 vector with H5 atom close to  $\text{Si}(\text{OH})_2$  surface facilitate the formation of hydrogen bonds between H5 and O atoms in  $\text{Si}(\text{OH})_2$  groups, as well as possible hydrogen bonded interactions between two nitrogen atoms of imidazolium rings and

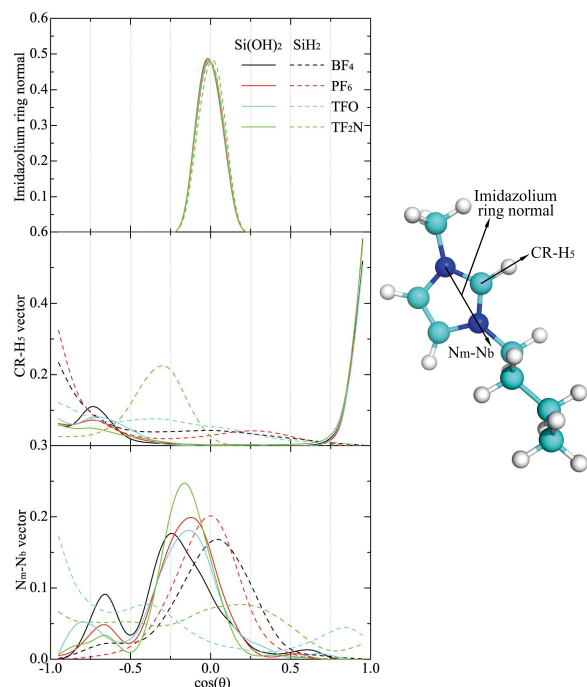


**Fig. 6** The probability distributions of specific vectors fixed in [BMIM] cation frame with respect to positive Z-axis in quartz interfacial region. These specific vectors are imidazolium ring normal (top panel), CR-H5 (middle panel) and Nm-Nb (bottom panel) vectors, respectively.

OH groups on  $\text{Si}(\text{OH})_2$  surface<sup>38,91</sup>. The secondary peaks in corresponding probability distribution profiles indicate that a minority of H5 atoms prefer to form hydrogen bonds with polar atoms in the corresponding paired anions, such as fluorine (F) atoms in four anions and O atoms in [TFO] and [TF<sub>2</sub>N] anions. In contrast, a strong formation of hydrogen bonds between [BMIM] cations and paired anions can be seen in  $\text{SiH}_2$  interfacial region. The most probable distribution of CR-H5 vector suggests that the angle between this vector and positive Z-axis is larger than 90°, implying that most H5 atoms are pointing into or close to the anionic layer on  $\text{SiH}_2$  surface, which can essentially contribute to the hydrogen bonded interactions between confined ion pairs.

The distinct orientation of imidazolium ring in quartz interfacial region further influences the orientational preferences of methyl and butyl chains of [BMIM] cations on  $\text{Si}(\text{OH})_2$  and  $\text{SiH}_2$  surfaces. The probability distributions of Nm-Cm and Nb-Cb vectors fixed in [BMIM] cation frame are calculated and presented in Fig. 8.

The sharp distribution of Nm-Cm vector in  $\text{Si}(\text{OH})_2$  interfacial region implies its tilted orientation with approximately 30° away from  $\text{Si}(\text{OH})_2$  surface, and corresponding methyl group close to surface, consistent with the number density of

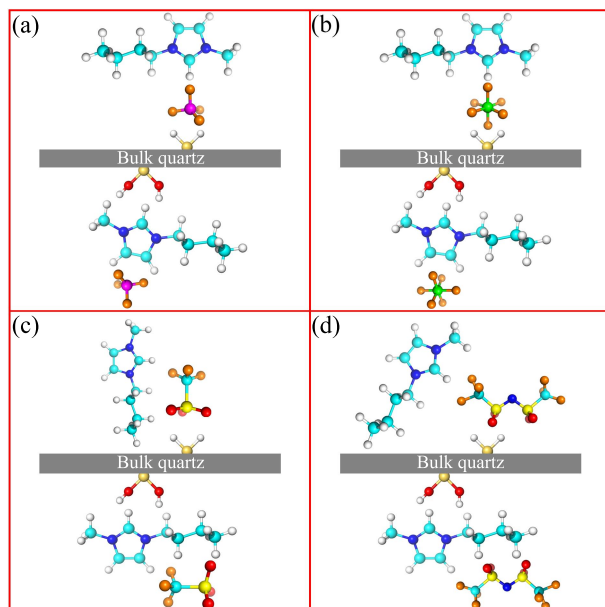


**Fig. 7** Representative configuration of confined ionic species in  $\text{Si}(\text{OH})_2$  (bottom surface) and  $\text{SiH}_2$  (top surface) interfacial region. (a) [BMIM][BF<sub>4</sub>]; (b) [BMIM][PF<sub>6</sub>]; (c) [BMIM][TFO]; (d) [BMIM][TF<sub>2</sub>N].

Cm atom shown in Fig. 3. The Nb-Cb vector is essentially parallel to  $\text{Si}(\text{OH})_2$  surface, consistent with the experimental SFG vibrational spectroscopy signature<sup>38</sup>, due to the relatively large volume of butyl chain compared to the space among adjacent drafted OH groups on  $\text{Si}(\text{OH})_2$  surface, and favorable interactions between butyl chain and  $\text{Si}(\text{OH})_2$  interfacial groups<sup>21,38</sup>.

However, the probability distributions of Nm-Cm and Nb-Cb vectors in  $\text{SiH}_2$  interfacial region are distinct and strongly related to ionic size and molecular geometry of anionic groups. In [BMIM][BF<sub>4</sub>] and [BMIM][PF<sub>6</sub>] simulation systems, Nm-Cm vector essentially takes parallel orientation along  $\text{SiH}_2$  surface. Meantime, the cosine value of the angle between Nb-Cb vector and positive Z-axis are negative, indicating that a majority of butyl chains take on tilted orientation with Cb atom pointing towards the anionic layer in  $\text{SiH}_2$  interfacial region. Both Nm-Cm and Nb-Cb vectors in [BMIM][TFO] simulation system are essentially perpendicular to  $\text{SiH}_2$  surface, with butyl chain pointing to  $\text{SiH}_2$  surface and methyl group pointing towards opposite direction, consistent with the perpendicular arrangement of Nm-Nb vector in  $\text{SiH}_2$  interfacial region. In [BMIM][TF<sub>2</sub>N] simulation system, the  $\text{SiH}_2$  surface is covered by [TF<sub>2</sub>N] anions owing to the relatively large anionic size, resulting in partially screened interactions between adsorbed imidazolium rings in subsequent cationic layer and  $\text{SiH}_2$  surface<sup>35</sup>, which lead to tilted distributions of Nm-Cm and Nb-Cb vectors in  $\text{SiH}_2$  interfacial region.

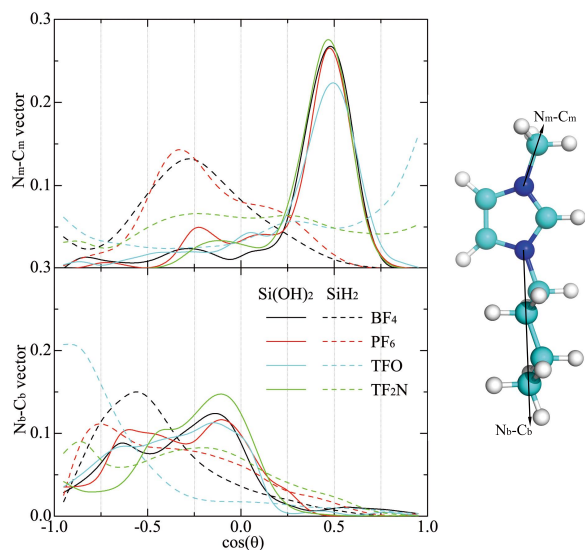


**Fig. 8** The probability distributions of Nm-Cm and Nb-Cb vectors fixed in [BMIM] cation frame with respect to positive Z-axis in quartz interfacial region.

Typical configuration of methyl and butyl chains of [BMIM] cations in  $\text{Si}(\text{OH})_2$  and  $\text{SiH}_2$  interfacial regions is shown in Fig. 7.

The effect of ionic size and molecular geometry of anionic groups, as well as quartz surface charge, on interfacial orientation of confined ILs is not only embodied in particular orientation of [BMIM] cations, but also presented in that of anions, especially for [TFO] and [TF<sub>2</sub>N] anions characterized with asymmetric molecular geometries. Fig. 9 presents the probability distributions of S-C vector in [TFO] and [TF<sub>2</sub>N] anions, as well as S-S vector in [TF<sub>2</sub>N] anion, respectively, in quartz interfacial region.

As [BMIM] cations exclusively attach onto  $\text{Si}(\text{OH})_2$  surface, the interactions between  $\text{Si}(\text{OH})_2$  surface and asymmetric anions are screened, which result in the average orientation of S-S and S-C vectors in  $\text{Si}(\text{OH})_2$  interfacial region. In  $\text{SiH}_2$  interfacial region, S-C vector in [TFO] anion exhibits perpendicular orientation with S atom close to solid surface, which is consistent with the number density distributions of S and C atoms shown in panel (d) of Fig. 3. For [TF<sub>2</sub>N] anion, the angles between S-C, S-S vectors and  $\text{SiH}_2$  surface are approximately 45° and 0°, respectively, indicating the aligned orientation of [TF<sub>2</sub>N] anion along  $\text{SiH}_2$  surface with  $\text{SO}_2$  groups locating between neighboring  $\text{SiH}_2$  groups due to the delocalized negative charges along S-N-S core. Such striking arrangement with O atoms close to  $\text{SiH}_2$  surface facilitates the hydrogen bonded interactions between  $\text{SiH}_2$  groups and absorbed [TF<sub>2</sub>N] anions. The distinct orientational preferences of asymmetric [TFO] and [TF<sub>2</sub>N] anions are rationalized by a

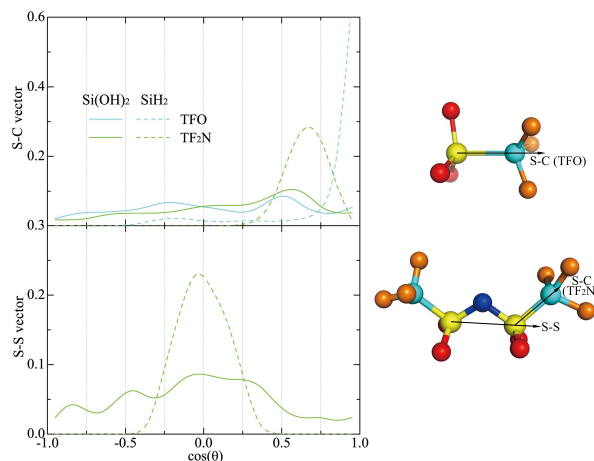


**Fig. 9** The probability distributions of S-C vector in [TFO] and [TF<sub>2</sub>N] anions and S-S vector in [TF<sub>2</sub>N] anion with respect to positive Z-axis in quartz interfacial region.

mismatch between anionic size and quartz interfacial structure, as reported in previous AFM experiments<sup>24,26,27,39,40</sup>. Typical configuration of absorbed [BF<sub>4</sub>], [PF<sub>6</sub>], [TFO] and [TF<sub>2</sub>N] anions in  $\text{Si}(\text{OH})_2$  and  $\text{SiH}_2$  interfacial regions is shown in Fig. 7.

The particular ionic structures of absorbed ILs in quartz interfacial region, which are distinct to the distribution and orientation of small molecules (such as water<sup>92–94</sup> and simple Lennard-Jones fluid<sup>95</sup>) on charged surfaces, are intrinsically related to ionic size and molecular geometry of anionic groups, as well as quartz surface charge. From this viewpoint, the understanding of the detailed balance between these individual contributions is important. On the industrial side, related studies can provide more insight in microlubrication and nanotribology since it is generally believed that the anti-wear properties of IL-based lubricants come from the formation of electric double-layer structure in solid interfacial region. On the fundamental side, the intrinsic interfacial structures of confined ILs provide an opportunity to study the double-layer effect at extremely high electrolyte concentration. Given the fact that ILs serve as both charged species and solvent molecules, larger ion concentration leads to smaller Debye length, indicating that electrostatic interactions are partially screened, and hence other effects become important, such as the so-called ion specific effect and crowding effect. The subtle interplay between screening and crowding effects contributes to the intrinsic distribution and orientation of confined ionic species in solid interfacial region<sup>88,96</sup>.

## 4 Summary and conclusion

Atomistic molecular dynamics simulations were performed to investigate microscopic interfacial structures and orientational preferences of absorbed ILs consisting of [BMIM] cations paired with four different anions ([BF<sub>4</sub>], [PF<sub>6</sub>], [TFO] and [TF<sub>2</sub>N]) on charged Si(OH)<sub>2</sub> and SiH<sub>2</sub> surfaces. Dense interfacial ionic layers, characterized by distinct mass, number, charge and electron density distributions, are formed in quartz interfacial region.

The detailed analyses of the probability distributions of various vectors reveal that confined [BMIM] cations and asymmetric [TFO] and [TF<sub>2</sub>N] anions exhibit different characteristics, depending on quartz surface charge, ionic size and molecular geometry of anionic groups. The [BMIM] cations exclusively attach onto Si(OH)<sub>2</sub> surface. The imidazolium rings lie predominantly perpendicular to Si(OH)<sub>2</sub> surface, with the corresponding methyl and butyl chains oriented towards and elongated along Si(OH)<sub>2</sub> surface, respectively. Four anions exhibit random orientations in subsequent anionic layer, due to the partially screened interactions between absorbed anions and Si(OH)<sub>2</sub> surface. In the SiH<sub>2</sub> interfacial region, anionic groups are particularly absorbed in interfacial region due to strong electrostatic interactions. The main axes of asymmetric [TFO] and [TF<sub>2</sub>N] anions are perpendicular and parallel to SiH<sub>2</sub> surface, respectively. The distinct orientational preferences of confined ILs attribute to the strong electrostatic interactions and the favorable hydrogen bonded interactions between absorbed ionic species and quartz interfacial groups.

## Acknowledgment

We gratefully acknowledge the financial support from the Swedish Science Council (VR). The computations were performed on resources provided by the Swedish National Infrastructure for Computing (SNIC) at HPC2N. We thank the e-COST via European network for ionic liquids and EXIL program (COST Action CM1206).

## References

- 1 B. E. Gurkan, J. C. de la Fuente, E. M. Mindrup, L. E. Ficke, B. F. Goodrich, E. A. Price, W. F. Schneider and J. F. Brennecke, *J. Am. Chem. Soc.*, 2010, **132**, 2116–2117.
- 2 J. W. Lee, J. Y. Shin, Y. S. Chun, H. B. Jang, C. E. Song and S. G. Lee, *Acc. Chem. Res.*, 2010, **43**, 985–994.
- 3 B. A. Rosen, A. Salehi-Khojin, M. R. Thorson, W. Zhu, D. T. Whipple, P. J. Kenis and R. I. Masel, *Science*, 2011, **334**, 643–644.
- 4 M. Gorlov and L. Kloo, *Dalton Trans.*, 2008, 2655–2666.
- 5 M. Armand, F. Endres, D. R. MacFarlane, H. Ohno and B. Scrosati, *Nature Mater.*, 2009, **8**, 621–629.
- 6 C. Ye, W. Liu, Y. Chen and L. Yu, *Chem. Commun.*, 2001, 2244–2245.
- 7 B. Phillips and J. Zabinski, *Tribol. Lett.*, 2004, **17**, 533–541.
- 8 F. Zhou, Y. Liang and W. Liu, *Chem. Soc. Rev.*, 2009, **38**, 2590–2599.
- 9 F. U. Shah, S. Glavatskih, D. R. MacFarlane, A. Somers, M. Forsyth and O. N. Antzutkin, *Phys. Chem. Chem. Phys.*, 2011, **13**, 12865–12873.
- 10 J. Sweeney, F. Hausen, R. Hayes, G. B. Webber, F. Endres, M. W. Rutland, R. Bennewitz and R. Atkin, *Phys. Rev. Lett.*, 2012, **109**, 155502.
- 11 O. Werzer, E. D. Cranston, G. G. Warr, R. Atkin and M. W. Rutland, *Phys. Chem. Chem. Phys.*, 2012, **14**, 5147–5152.
- 12 F. U. Shah, S. Glavatskih and O. N. Antzutkin, *Tribol. Lett.*, 2013, **51**, 281–301.
- 13 J. L. Anderson, D. W. Armstrong and G. T. Wei, *Anal. Chem.*, 2006, **78**, 2892–2902.
- 14 X. Han and D. W. Armstrong, *Acc. Chem. Res.*, 2007, **40**, 1079–1086.
- 15 A. Rout, S. Wellens and K. Binnemans, *RSC Adv.*, 2014, **4**, 5753–5758.
- 16 S. Chen, G. Wu, M. Sha and S. Huang, *J. Am. Chem. Soc.*, 2007, **129**, 2416–2417.
- 17 M. Mezger, H. Schröder, H. Reichert, S. Schramm, J. S. Okasinski, S. Schöder, V. Honkimäki, M. Deutsch, B. M. Ocko and J. Ralston, *Science*, 2008, **322**, 424–428.
- 18 S. Chen, K. Kobayashi, Y. Miyata, N. Imazu, T. Saito, R. Kitaura and H. Shinohara, *J. Am. Chem. Soc.*, 2009, **131**, 14850–14856.
- 19 Y. Liu, G. Wu, H. Fu, Z. Jiang, S. Chen and M. Sha, *Dalton Trans.*, 2010, **39**, 3190–3194.
- 20 L. Rodríguez-Pérez, Y. Coppel, I. Favier, E. Teuma, P. Serp and M. Gómez, *Dalton Trans.*, 2010, **39**, 7565–7568.
- 21 M. P. Singh, R. K. Singh and S. Chandra, *J. Phys. Chem. B*, 2011, **115**, 7505–7514.
- 22 S. Chen, Y. Liu, H. Fu, Y. He, C. Li, W. Huang, Z. Jiang and G. Wu, *J. Phys. Chem. Lett.*, 2012, **3**, 1052–1055.
- 23 J. Im, S. D. Cho, M. H. Kim, Y. M. Jung, H. S. Kim and H. S. Park, *Chem. Commun.*, 2012, **48**, 2015–2017.
- 24 X. Gong, S. Frankert, Y. Wang and L. Li, *Chem. Commun.*, 2013, **49**, 7803–7805.
- 25 A. N. Khlobystov, D. A. Britz and G. A. D. Briggs, *Acc. Chem. Res.*, 2005, **38**, 901–909.
- 26 R. Atkin and G. G. Warr, *J. Phys. Chem. C*, 2007, **111**, 5162–5168.
- 27 S. Bovio, A. Podesta, P. Milani, P. Ballone and M. G. Del Pópolo, *J. Phys.: Condens. Matter*, 2009, **21**, 424118.

- 28 T. J. Gannon, G. Law, P. R. Watson, A. J. Carmichael and K. R. Seddon, *Langmuir*, 1999, **15**, 8429–8434.
- 29 G. Law, P. R. Watson, A. J. Carmichael and K. R. Seddon, *Phys. Chem. Chem. Phys.*, 2001, **3**, 2879–2885.
- 30 J. Bowers, M. C. Vergara-Gutierrez and J. R. Webster, *Langmuir*, 2004, **20**, 309–312.
- 31 E. Sloutskin, B. M. Ocko, L. Tamam, I. Kuzmenko, T. Gog and M. Deutsch, *J. Am. Chem. Soc.*, 2005, **127**, 7796–7804.
- 32 P. Niga, D. Wakeham, A. Nelson, G. G. Warr, M. Rutland and R. Atkin, *Langmuir*, 2010, **26**, 8282–8288.
- 33 Y. Lauw, M. D. Horne, T. Rodopoulos, V. Lockett, B. Akgun, W. A. Hamilton and A. R. Nelson, *Langmuir*, 2012, **28**, 7374–7381.
- 34 S. Baldelli, *J. Phys. Chem. B*, 2003, **107**, 6148–6152.
- 35 B. D. Fitchett and J. C. Conboy, *J. Phys. Chem. B*, 2004, **108**, 20255–20262.
- 36 S. Rivera-Rubero and S. Baldelli, *J. Am. Chem. Soc.*, 2004, **126**, 11788–11789.
- 37 S. Rivera-Rubero and S. Baldelli, *J. Phys. Chem. B*, 2006, **110**, 4756–4765.
- 38 C. Romero and S. Baldelli, *J. Phys. Chem. B*, 2006, **110**, 6213–6223.
- 39 J. B. Rollins, B. D. Fitchett and J. C. Conboy, *J. Phys. Chem. B*, 2007, **111**, 4990–4999.
- 40 C. Romero, H. J. Moore, T. R. Lee and S. Baldelli, *J. Phys. Chem. C*, 2007, **111**, 240–247.
- 41 C. S. Santos, S. Rivera-Rubero, S. Dibrov and S. Baldelli, *J. Phys. Chem. C*, 2007, **111**, 7682–7691.
- 42 S. Baldelli, *J. Phys. Chem. Lett.*, 2012, **4**, 244–252.
- 43 N. Sieffert and G. Wipff, *J. Phys. Chem. C*, 2008, **112**, 19590–19603.
- 44 N. N. Rajput, J. Monk, R. Singh and F. R. Hung, *J. Phys. Chem. C*, 2012, **116**, 5169–5181.
- 45 Y.-L. Wang, A. Laaksonen and Z.-Y. Lu, *Phys. Chem. Chem. Phys.*, 2013, **15**, 13559–13569.
- 46 J. Vatamanu, O. Borodin and G. D. Smith, *J. Am. Chem. Soc.*, 2010, **132**, 14825–14833.
- 47 J. Forsman, C. E. Woodward and M. Trulsson, *J. Phys. Chem. B*, 2011, **115**, 4606–4612.
- 48 C. Merlet, M. Salanne, B. Rotenberg and P. A. Madden, *J. Phys. Chem. C*, 2011, **115**, 16613–16618.
- 49 M. Turesson, R. Szparaga, K. Ma, C. E. Woodward and J. Forsman, *Soft Matter*, 2014, **10**, 3229–3237.
- 50 K. Dong, G. Zhou, X. Liu, X. Yao, S. Zhang and A. Lyubartsev, *J. Phys. Chem. C*, 2009, **113**, 10013–10020.
- 51 S. Wang, S. Li, Z. Cao and T. Yan, *J. Phys. Chem. C*, 2009, **114**, 990–995.
- 52 Y. Liu, Y. Zhang, G. Wu and J. Hu, *J. Am. Chem. Soc.*, 2006, **128**, 7456–7457.
- 53 S. Perkin, T. Albrecht and J. Klein, *Phys. Chem. Chem. Phys.*, 2010, **12**, 1243–1247.
- 54 S. Perkin, L. Crowhurst, H. Niedermeyer, T. Welton, A. M. Smith and N. N. Gosvami, *Chem. Commun.*, 2011, **47**, 6572–6574.
- 55 S. Perkin, *Phys. Chem. Chem. Phys.*, 2012, **14**, 5052–5062.
- 56 H. Zhou, M. Rouha, G. Feng, S. S. Lee, H. Docherty, P. Fenter, P. T. Cummings, P. F. Fulvio, S. Dai and J. McDonough, *ACS Nano*, 2012, **6**, 9818–9827.
- 57 H. J. Castejón, T. J. Wynn and Z. M. Marcin, *J. Phys. Chem. B*, 2014, **118**, 3661–3668.
- 58 C.-M. Yang, Y.-J. Kim, M. Endo, H. Kanoh, M. Yudasaka, S. Iijima and K. Kaneko, *J. Am. Chem. Soc.*, 2007, **129**, 20–21.
- 59 E. Uesugi, H. Goto, R. Eguchi, A. Fujiwara and Y. Kubozono, *Sci. Rep.*, 2013, **3**, 1595.
- 60 Z. Yu, N. Vlachopoulos, A. Hagfeldt and L. Kloo, *RSC Adv.*, 2013, **3**, 1896–1901.
- 61 R. Guégan, D. Morineau and C. Alba-Simionesco, *Chem. Phys.*, 2005, **317**, 236–244.
- 62 C. Aliaga, C. S. Santos and S. Baldelli, *Phys. Chem. Chem. Phys.*, 2007, **9**, 3683–3700.
- 63 S. Li, K. S. Han, G. Feng, E. W. Hagaman, L. Vlcek and P. T. Cummings, *Langmuir*, 2013, **29**, 9744–9749.
- 64 K. Shimizu, A. Pensado, P. Malfreyt, A. A. Pádua and J. N. C. Lopes, *Faraday Discuss.*, 2012, **154**, 155–169.
- 65 F. F. Canova, H. Matsubara, M. Mizukami, K. Kurihara and A. L. Shluger, *Phys. Chem. Chem. Phys.*, 2014, **16**, 8247–8256.
- 66 B. Ewers and J. Batteas, *RSC Adv.*, 2014, **4**, 16803–16812.
- 67 G. Ori, F. Villemot, L. Viau, A. Vioux and B. Coasne, *Mol. Phys.*, 2014, **112**, 1350–1361.
- 68 R. K. Iler, *The chemistry of silica: solubility, polymerization, colloid and surface properties, and biochemistry*, Wiley, 1979.
- 69 K. Yamaguchi, C. Yoshida, S. Uchida and N. Mizuno, *J. Am. Chem. Soc.*, 2005, **127**, 530–531.
- 70 Q. Wang, G. A. Baker, S. N. Baker and L. A. Colón, *Analyst*, 2006, **131**, 1000–1005.
- 71 K. B. Sidhpuria, A. L. Daniel-da Silva, T. Trindade and J. A. Coutinho, *Green Chem.*, 2011, **13**, 340–349.
- 72 P. E. M. Lopes, V. Murashov, M. Tazi, E. Demchuk and A. D. MacKerell, *J. Phys. Chem. B*, 2006, **110**, 2782–2792.
- 73 M. J. Frisch, G. W. Trucks, H. B. Schlegel, G. E. Scuseria, M. A. Robb, J. R. Cheeseman, G. Scalmani, V. Barone, B. Mennucci, G. A. Petersson, H. Nakatsuji, M. Caricato, X. Li, H. P. Hratchian, A. F. Izmaylov, J. Bloino, G. Zheng,

- J. L. Sonnenberg, M. Hada, M. Ehara, K. Toyota, R. Fukuda, J. Hasegawa, M. Ishida, T. Nakajima, Y. Honda, O. Kitao, H. Nakai, T. Vreven, J. A. Montgomery Jr., J. E. Peralta, F. Ogliaro, M. Bearpark, J. J. Heyd, E. Brothers, K. N. Kudin, V. N. Staroverov, R. Kobayashi, J. Normand, K. Raghavachari, A. Rendell, J. C. Burant, S. S. Iyengar, J. Tomasi, M. Cossi, N. Rega, J. M. Millam, M. Klene, J. E. Knox, J. B. Cross, V. Bakken, C. Adamo, J. Jaramillo, R. Gomperts, R. E. Stratmann, O. Yazyev, A. J. Austin, R. Cammi, C. Pomelli, J. W. Ochterski, R. L. Martin, K. Morokuma, V. G. Zakrzewski, G. A. Voth, P. Salvador, J. J. Dannenberg, S. Dapprich, A. D. Daniels, O. Farkas, J. B. Foresman, J. V. Ortiz, J. Cioslowski and D. J. Fox, *Gaussian: Wallingford, CT, USA*, 2009.
- 74 Z. Liu, S. Huang and W. Wang, *J. Phys. Chem. B*, 2004, **108**, 12978–12989.
- 75 X. Zhong, Z. Liu and D. Cao, *J. Phys. Chem. B*, 2011, **115**, 10027–10040.
- 76 X. Wu, Z. Liu, S. Huang and W. Wang, *Phys. Chem. Chem. Phys.*, 2005, **7**, 2771–2779.
- 77 Y.-L. Wang, A. Lyubartsev, Z.-Y. Lu and A. Laaksonen, *Phys. Chem. Chem. Phys.*, 2013, **15**, 7701–7712.
- 78 A. Lyubartsev and A. Laaksonen, *Comput. Phys. Commun.*, 2000, **128**, 565–589.
- 79 M. Tuckerman, B. J. Berne and G. J. Martyna, *J. Chem. Phys.*, 1992, **97**, 1990.
- 80 P. Ballone, M. Del Pópolo, S. Bovio, A. Podestà, P. Milani and N. Manini, *Phys. Chem. Chem. Phys.*, 2012, **14**, 2475–2482.
- 81 X.-G. Xue, L. Zhao, Z.-Y. Lu and H.-J. Qian, *Chem. Res. Chin. Univ.*, 2013, **29**, 366–373.
- 82 Y.-L. Wang, Z.-Y. Lu and A. Laaksonen, DOI: 10.1039/C4CP02843K, 2014.
- 83 S. A. Kislenko, I. S. Samoylov and R. H. Amirov, *Phys. Chem. Chem. Phys.*, 2009, **11**, 5584–5590.
- 84 Q. Dou, M. Sha, H. Y. Fu and G. Wu, *J. Phys.: Condens. Matter*, 2011, **23**, 175001.
- 85 R. M. Lynden-Bell, A. Frolov and M. V. Fedorov, *Phys. Chem. Chem. Phys.*, 2012, **14**, 2693–2701.
- 86 M. Sobota, I. Nikiforidis, W. Hieringer, N. Paape, M. Hoppel, H.-P. Steinrück, A. Görling, P. Wasserscheid, M. Laurin and J. Libuda, *Langmuir*, 2010, **26**, 7199–7207.
- 87 S. Baldelli, *J. Phys. Chem. B*, 2005, **109**, 13049–13051.
- 88 M. Z. Bazant, B. D. Storey and A. A. Kornyshev, *Phys. Rev. Lett.*, 2011, **106**, 046102.
- 89 A. J. Carmichael, C. Hardacre, J. D. Holbrey, M. Nieuwenhuyzen and K. R. Seddon, *Mol. Phys.*, 2001, **99**, 795–800.
- 90 S. Zhang, N. Sun, X. He, X. Lu and X. Zhang, *J. Phys. Chem. Ref. Data*, 2006, **35**, 1475–1517.
- 91 G. Law and P. R. Watson, *Chem. Phys. Lett.*, 2001, **345**, 1–4.
- 92 C. Wang, H. Lu, Z. Wang, P. Xiu, B. Zhou, G. Zuo, R. Wan, J. Hu and H. Fang, *Phys. Rev. Lett.*, 2009, **103**, 137801.
- 93 A. Phan, T. A. Ho, D. Cole and A. Striolo, *J. Phys. Chem. C*, 2012, **116**, 15962–15973.
- 94 C. Wang, B. Zhou, Y. Tu, M. Duan, P. Xiu, J. Li and H. Fang, *Sci. Rep.*, 2012, **2**, 358.
- 95 X. Yong and L. T. Zhang, *Phys. Rev. E*, 2010, **82**, 056313.
- 96 A. A. Kornyshev, *J. Phys. Chem. B*, 2007, **111**, 5545–5557.